



Free Motion around Black Holes with Disks or Rings: Between Integrability and Chaos–V

L. Polcar^{1,2}, P. Suková² , and O. Semerák¹ 

¹ Institute of Theoretical Physics, Faculty of Mathematics and Physics, Charles University, Prague, Czechia; oldrich.semerak@mff.cuni.cz

² Astronomical Institute, Czech Academy of Sciences, Ondřejov, Czechia; petra.sukova@asu.cas.cz

Received 2019 January 18; revised 2019 April 2; accepted 2019 April 10; published 2019 May 17

Abstract

The complete integrability of geodesic motion, the well-known feature of fields of isolated stationary black holes, can easily be “spoiled” by the presence of some additional sources (even if highly symmetric). In previous papers, we used various methods to show how free time-like motion becomes chaotic if the gravitational field of the Schwarzschild black hole is perturbed by that of a circular disk or ring, considering specifically the inverted first disk of the Morgan–Morgan counter-rotating family and the Bach–Weyl ring as additional sources. The present paper focuses on two new points. First, because the Bach–Weyl thin ring is physically quite unsatisfactory, we now repeat some of the analyses for a different, Majumdar–Papapetrou-type (extremally charged) ring around an extreme Reissner–Nordström black hole, and compare the results with those obtained before. We also argue that such a system is in fact more relevant astrophysically than it may seem. Second, we check numerically, for the latter system as well as for the Schwarzschild black hole encircled by the inverted Morgan–Morgan disk, how indicative the geometric (curvature) criterion is for the chaos suggested by Sota et al. We also add a review of the literature where the relevance of geometric criteria in general relativity (as well as elsewhere) has been discussed for decades.

Key words: black hole physics – chaos – gravitation – relativistic processes

1. Introduction

When studying a dynamical system, it goes without saying that the question of how the features of its evolution are related to the properties of the governing interaction is asked. Depending on the characteristics of the interaction, it is sometimes possible to interpret the dynamics as a geodesic flow in an effective manifold endowed with a metric obtained by a certain rescaling from the original, “physical” one (Anosov & Sinai 1967; Szydłowski 1994); general relativity theory itself stands as a celebrated example of such a “geometrization” of an interaction.³ If the latter has been achieved, the question of to what extent the features of the system’s dynamics follow from the quasi-local geometry of the obtained manifold naturally arises. A firm answer was given by Vieira & Letelier (1996b, p. 3119): while admitting that there surely exist links between global dynamics and local (curvature) properties of the corresponding configuration manifold of the system, they pointed out that “any local analysis, in effective or even physical spaces, is far from being sufficient to predict a global phenomenon like chaotic motion” (more recently, the same statement has been voiced by, e.g., Stránský & Cejnar 2015). One can easily imagine, for example, a system living in a Euclidean space and subject to an interaction only acting at discrete locations (and/or times), such as, e.g., collisions of a ball with an obstacle. In such a case, the (plane) geometry at that generic location cannot alone tell anything about whether, when, and with what result the ball is to hit a pole.

However, a general-relativistic spacetime is not discrete in the above sense, because any source (mass–energy) is felt everywhere in it, not just at specific locations. More accurately, one would be better off restricting to stationary spacetimes,

because, in a causal theory, changes are being “announced” with at most the speed of light, not immediately; so, for instance, a gravitational wave is in fact always “surprising” and cannot be anticipated from how the geometry at a given location looks “now” (the geometry can even be flat both before and after the wave). In a stationary case, the local geometry at any place and time is interconnected with how it looks elsewhere, so one may hope that when studying the evolution of some system in such a background, the local geometry could provide enough information to predict the character of the system’s global dynamics. This hope has been strongly supported by observation (Anosov & Sinai 1967) that the geodesic flow is chaotic in manifolds whose sectional curvatures are negative everywhere. Unfortunately, the result is only guaranteed for compact manifolds without a boundary, while in real situations the accessible region often has some boundary, which also affects the geodesic flow (there, the effective “Jacobi” metric typically has a singularity).

Another reason to hope for the plausibility of geometric criteria in the study of geodesic flow in spacetime is that in this case, one does not (or need not) refer to any effective manifold—the geometry of the original, “physical” configuration space itself is relevant. Within general relativity, the geometric criteria have notably been studied by Szydłowski and coworkers in the 1990s (see Szydłowski 1993; Biesiada 1995; Szydłowski & Krawiec 1996, for example). Yurtsever (1995) checked their reliability in the specific background of a Majumdar–Papapetrou (MP)-type binary of extremally charged static black holes (see also Szydłowski 1997). He showed that null geodesics in this background can be treated as spatial geodesics on a certain two-dimensional Riemann surface and that the Gauss curvature of this surface is everywhere negative for any mass of the two black holes. The null geodesic flow can thus be expected to be chaotic, because the negative curvature of a surface spanned by the flow is known to correspond to the

³ Gravitation, in particular, is a universal interaction, so it can be attributed to an underlying “stage” independently of a specific situation, while still keeping the stage dynamic.

exponential divergence of the geodesics (the flow has positive Lyapunov exponents). However, Yurtsever (1995) asked then whether such properties (implying “sensitive dependence on initial conditions”) are not only necessary, but also sufficient for the occurrence of chaos, and answered that negatively, pointing out that the flow must in addition be “topologically mixing” (mixing phase-space regions). He finished by demonstrating that the considered null geodesic flow does have the mixing property as well.

Soon after, Sota et al. (1996) studied the geodesic dynamics in several static axisymmetric spacetimes, namely those of the Zipoy–Vorhees class describing the fields of finite axial rods (and including, e.g., the Schwarzschild and Curzon metrics as special cases) and also those generated by a system of Curzon-type point singularities distributed along the symmetry axis. The main focus was to compare standard methods like Poincaré maps, Lyapunov exponents, or the detection of a homoclinic tangle (which indicates chaos in the above situations) with criteria based on curvature properties of the spacetime background. Specifically, they studied tidal-matrix eigenvalues and the curvature of the fictitious space obtained by energy-dependent conformal mapping within the Newtonian approach, and the eigenvalues of a matrix obtained from the Weyl tensor in the relativistic case. Vieira & Letelier (1996b) then demonstrated, however, that the curvature criterion suggested by Sota et al. (1996) is neither necessary nor sufficient for the occurrence of chaos, and showed that the disputed conclusion (about the sufficiency of the proposed criterion) was probably made due to wrong judgement about the nonhomoclinic character of a certain mode of chaotic behavior that had been observed.

Szczyński & Dobrowolski (1999) provided a useful summary of the reasoning based on the Maupertuis–Lagrange–Jacobi principle, the connection between the interaction potential, the system’s energy and the effective-metric curvature, the equation of geodesic deviation, and the Lyapunov exponents of the flow. They demonstrated using examples of how such a reasoning naturally provides a geometric criterion for local stability of the flow, but reminded that such a criterion could only be successful if the evolution were confined, within the effective Riemannian manifold, to a compact region without boundary. Later, Saa (2004) illustrated the problem with the influence of the boundary on a system whose Jacobi-metric Gaussian curvature is everywhere positive in the accessible-region interior, but which is still chaotic, due to trajectories that “bounce off” the nonconvex part of the boundary (like in famous billiard problems). Szydlowski et al. (1996) suggested how to possibly circumvent this problem by releasing the smoothness of the manifold.

In the meantime, Ramasubramanian & Sriram (2001, see also references therein) confirmed, on several Hamiltonian systems with two degrees of freedom, that the average sectional curvature defined by the effective-manifold geodesic congruence is closely related to the square of the average value of the maximal Lyapunov exponent, and conjectured a linear relation between these two quantities for Hamiltonian systems in general. Nevertheless, they pointed out that the above sectional curvature does not provide a sufficiently accurate indicator of the order–chaos transition.

For another direction of objections against the generic reliability of “geometric criteria for chaos,” see, e.g., Wu (2009) and references given therein: it turns out that chaotic evolution may even be the case if the effective-manifold curvature is positive, but varying with position. The likely mechanism is the parametric

instability, due to some kind of resonance between the characteristics of the background curvature and those of the geodesic flow.

The purpose of the present paper is to further study the astrophysically motivated problem of motion of free test particles in static and axially symmetric fields generated by black holes surrounded by thin rings or disks. In previous papers, we used several different methods to reveal how the time-like geodesic flow becomes chaotic as a function of the parameters of the system (the relative mass of the external source and particle energy, in particular). In Semerák & Suková (2010), we employed Poincaré sections, time series of position and velocity and their power spectra, and time evolution of the orbital “latitudinal action.” In Semerák & Suková (2012), we classified the orbits according to the shape of the time-series power spectra, and also by applying two recurrence methods, one based on tracing directions in which the trajectory recurrently passes through a preselected mesh of phase-space cells, and the other based on statistics over the recurrences themselves. In Suková & Semerák (2013), we computed several Lyapunov-type coefficients that quantify the rate of orbital divergence, namely the maximal Lyapunov characteristic exponent and indicators called the fast Lyapunov indicator (FLI) and MEGNO (in that paper, we specifically considered a system involving a black hole surrounded by a small thin “accretion” disk or a large ring, having in mind the configuration that is observed in some galactic nuclei). Finally, in Witzany et al. (2015), we compared the above exact, general-relativistic treatment of the system with the Newtonian one, which mainly involved testing several “pseudo-Newtonian” potentials to mimic the central black hole.

In the present paper, we check, on time-like geodesics in our black hole–disk/ring field again, how indicative is the curvature criterion suggested by Sota et al. (1996). Led by a Newtonian case where the local convergence/divergence of neighboring trajectories is correlated with the sign of the eigenvalues of the tidal matrix (given by the second derivatives of the gravitational potential), Sota et al. (1996) followed the above quoted results by Szydlowski et al. and considered a local criterion based on certain eigenvalues of the Riemann tensor. After a short summary of the criterion in Section 2, we compare its guess with a numerical study of the actual geodesic flow in Section 5.

Aside from the above aim, we also include one novelty, namely, when considering the thin ring placed around a black hole in a concentric way, we choose a solution different from previous papers of this series. There, we took the aged Bach–Weyl (BW) solution (Bach & Weyl 1922) which is considered the default solution of this type as it corresponds to a Newtonian homogeneous-ring solution for the potential (ν), supplemented by an appropriate second metric function λ according to the field equations. However, we showed in Semerák (2016) that the BW ring is a rather strange source, mainly in that its field is not locally cylindrical (the ring is infinitely remote “from within,” whereas at finite distance “from outside”). We compared it with several other ring-singularity solutions there and found, in particular, that the field generated by what we called the MP ring, namely a homogeneous circular thin ring bearing an extremal value of electric charge (its density equals the mass density), is physically much more reasonable (not directional, in particular). Thanks to an exact balance between gravitational attraction and electrostatic repulsion, solutions of this kind are known to provide one of the rare options for multibody

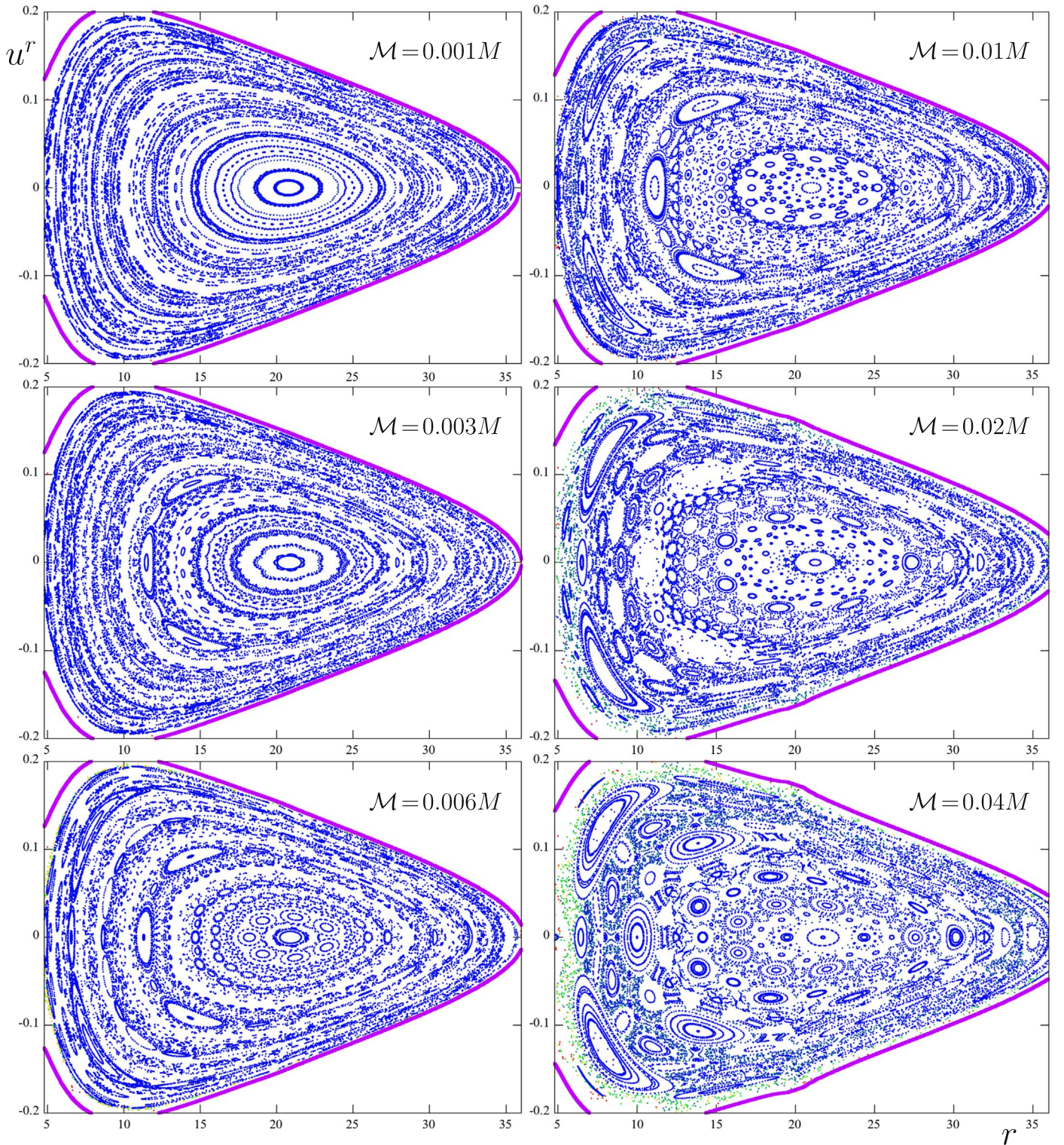


Figure 1. Equatorial Poincaré sections for geodesics in the field of a Schwarzschild black hole encircled by a Bach–Weyl ring with radius $r_{\text{ring}} = 20 M$: dependence on relative ring mass \mathcal{M}/M (its value is indicated in the plots). Passages of orbits having $\ell = 3.75 M$, $\mathcal{E} = 0.977$ through the ring plane are drawn. See the main text for a description of the coloring.

equilibria (and even the only option for equilibria of multiple black holes). Within the class of MP solutions, the superposition is very simple—in particular, the function λ remains zero, so we also choose the extreme Reissner–Nordström (RN) black hole (which is the MP-type source as well) instead of the Schwarzschild one as the central body.

Note that we use geometrized units in which $c = 1$ and $G = 1$, and the metric signature $(-+++)$. The convention for the Riemann curvature tensor $R^\mu{}_{\nu\kappa\lambda}$ is given by the Ricci identity for the commutator of covariant derivatives, $V_{\nu;\kappa\lambda} - V_{\nu;\lambda\kappa} = R^\mu{}_{\nu\kappa\lambda} V_\mu$. Greek indices represent spacetime components (0, 1, 2, 3). We set the cosmological constant to zero. Let us also stress here that we

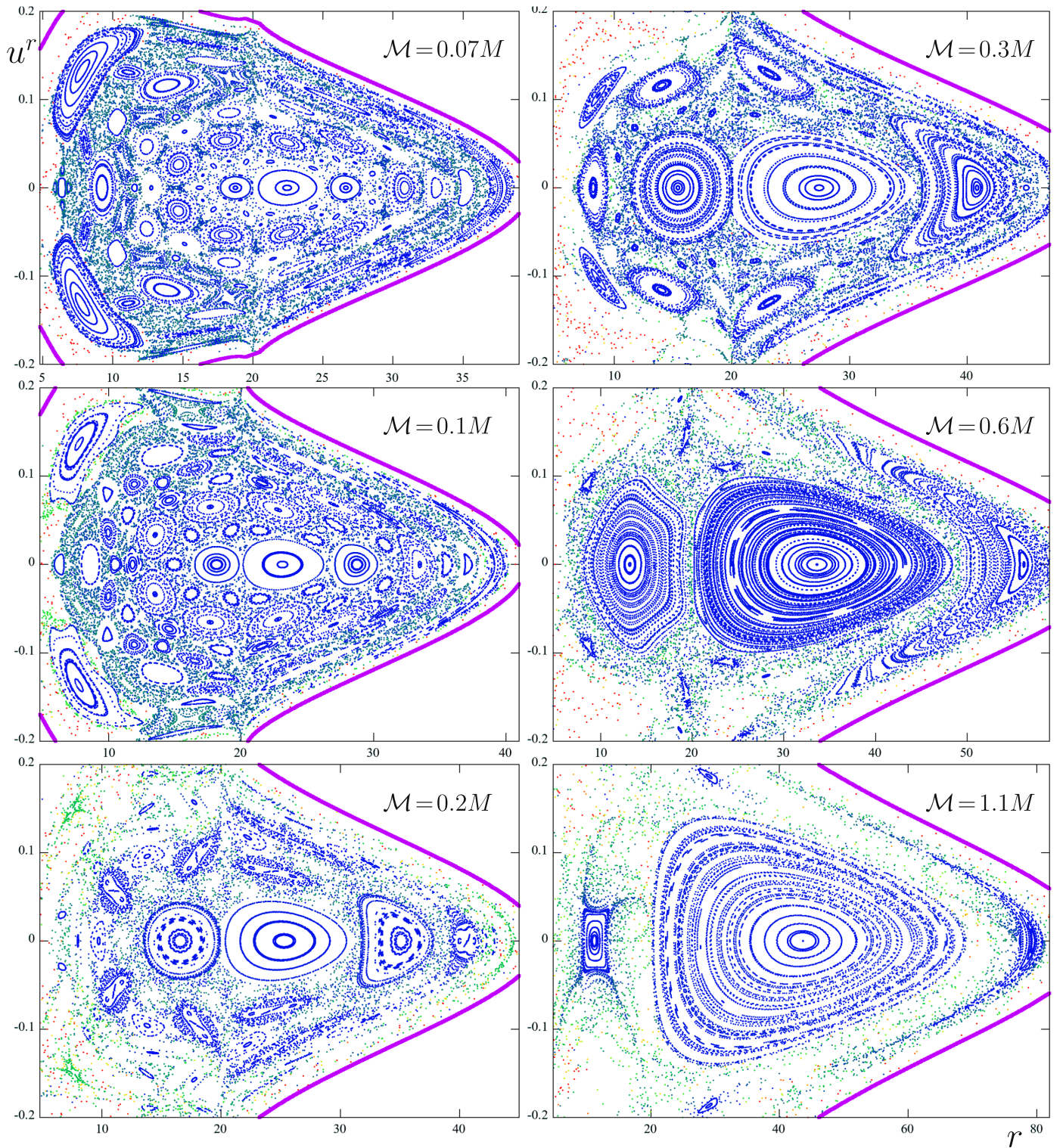


Figure 1. (Continued.)

study just geodesic motion in the above spacetimes, that is, the test particles only interact with the disk gravitationally (if crossing the disk, they do not interact mechanically, in particular).

1.1. Note on Extremally Charged Sources

Because it is always stressed that extremally charged sources have zero astrophysical relevance, we should explain more why

we have included them in this study. As already mentioned above, the main reason is that the exact general-relativistic gravitational field (and mainly curvature) behaves much more reasonably in the vicinity of the MP ring than around the BW ring (Semerák 2016). Actually, though the BW ring is a straightforward counterpart of the Newtonian circular ring, it turns out to be a directional singularity—it behaves differently when approached from different local meridional directions,

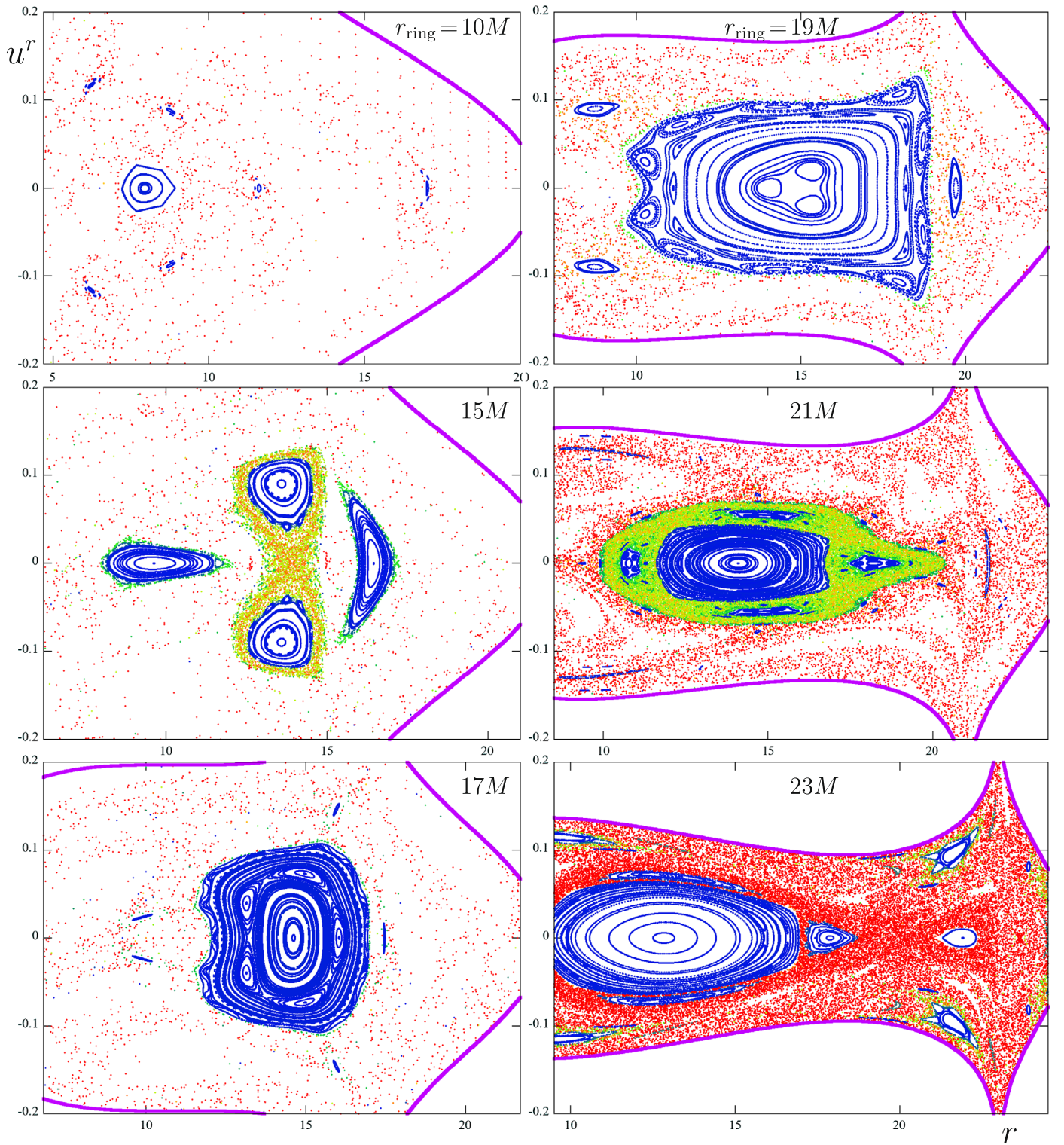


Figure 2. Poincaré diagrams of similar type to those in Figure 1, now showing the dependence of geodesic dynamics on radius of the BW ring r_{ring} (its values are again given in the plots). The ring mass is set at $\mathcal{M} = 0.5 M$, and the geodesics have constants of motion $\ell = 3.75 M$, $\mathcal{E} = 0.94$.

even lying at infinite proper distance when approached from within. Besides being rather unacceptable as a model of an astrophysical ring (thin toroid), we also suspected that it is just this weird property that might induce geodesic chaos in our system, so we needed to employ a more reasonable ring source to verify this—and the MP-type ring is the only other static

circular thin ring that is available. (We focus on the comparison of the two configurations in Section 4.)

Needless to say, we are not saying that astrophysical sources are significantly charged. However, being charged is in fact a good rather than bad feature of the configuration we newly included, because the electromagnetic field that it

brings along may mimic the gravitational effect of diluted matter in the system, namely that real accreting black hole systems are not in vacuum, but rather immersed in gas. Although the electromagnetic field is of course a different source than gas, it has the same main property—a positive mass–energy density. This property is in fact the only important one in our case, because we are interested in the motion of uncharged particles, which only feel the gravitational effect of the sources (including that of their electromagnetic field); they do not feel the Lorentz force. One can add that the electromagnetic-field energy density even behaves in a desirable way in that it is maximal at the sources (black hole and the ring) and falls off when receding from them, like what one could expect for a gaseous environment. More specifically, for the MP family of solutions, the electrostatic potential Φ is related to the gravitational potential ν in a very simple way, $\Phi = e^\nu + \text{const}$.

To summarize this point, it is because of physical reasons, not just to study “yet another source,” that we consider charged sources here. We are far from claiming that accreting black holes are properly described by extremally charged configurations; we only claim that the configuration we have newly included here can describe the gravitational field of accreting black holes more adequately than the superposition of a Schwarzschild black hole with the BW ring which we used in previous papers of this series.

2. Geometric Criterion Based on Eigenvalues of the Riemann Tensor

Following Sota et al. (1996), let us rewrite the geodesic deviation equation for a tangent field u^μ and a transversal relative position n^μ (supposed to be orthogonal, $u_\mu n^\mu = 0$) as

$$\begin{aligned} \frac{D^2 n^\mu}{d\tau^2} &= -R^\mu{}_{\nu\kappa\lambda} u^\nu n^\kappa u^\lambda \\ &= -\frac{1}{2} g^{\mu\nu} \frac{\partial}{\partial n^\nu} (R_{\alpha\beta\gamma\delta} n^\alpha u^\beta n^\gamma u^\delta) \\ &= -\frac{1}{2} g^{\mu\nu} \frac{\partial}{\partial n^\nu} (E_\gamma^\alpha n_\alpha n^\gamma), \end{aligned} \quad (1)$$

where $E_\gamma^\alpha := R^{\alpha\beta}{}_{\gamma\delta} u_\beta u^\delta$ is the “electric” part of the Riemann/Weyl tensor (in the frame tied to u^μ) and $D/d\tau$ is the absolute derivative along u^μ , with τ denoting proper time. The expression $\frac{1}{2} E_\gamma^\alpha n_\alpha n^\gamma$ clearly represents a kind of tidal-force potential. This potential has a saddle point (with zero value) at $n^\mu = 0$, and its behavior in the vicinity of this point tells in which n^μ directions the geodesics converge/diverge. Which of the two tendencies prevails can be learned from the eigenvalues of E_γ^α .

Because the energy–momentum tensor of an electromagnetic field is traceless and we do not consider any other source (and assume zero cosmological constant), the Einstein equations imply zero Ricci scalar and this in turn means that the tensor E_γ^α is traceless in a vacuum. As a 4×4 matrix, E_γ^α has four eigenvalues; the sum of these is zero due to the zero trace (in the vacuum). Also, one of the eigenvalues is zero, namely that

corresponding to the eigendirection given by u^γ ,

$$E_\gamma^\alpha u^\gamma = R^{\alpha\beta}{}_{\gamma\delta} u_\beta u^\delta u^\gamma = 0.$$

However, n^γ never belongs to this eigensubspace, because it is orthogonal to u^γ . Hence, the remaining three eigenvalues are relevant.

The electric part of the Riemann tensor is dependent on the four-velocity u^μ which, however, is not known a priori (there is no analytical formula for it). Nevertheless, it has been shown (see Sota et al. 1996) that the nonzero eigenvalues of E_γ^α solve the related eigenproblem as well,

$$R_B^A S^B = \kappa S^A, \quad (2)$$

where S^A is a column vector associated with the bivector $S^{\mu\nu} = n^\mu u^\nu - u^\mu n^\nu$, and R_B^A is a 6×6 matrix that represents the action of the Riemann tensor on the space of bivectors. The matrix R_B^A has in total six eigenvalues, and fixing the u^μ in $S^{\mu\nu}$ exactly selects the three that are also eigenvalues of E_γ^α .

Consider now the Weyl metric,

$$ds^2 = -N^2 dt^2 + N^{-2} [\rho^2 d\phi^2 + e^{2\lambda} (d\rho^2 + dz^2)], \quad (3)$$

where t and ϕ are Killing coordinates (on which the metric does not depend), so the two metric functions $N \equiv e^\nu$ (lapse) and λ only depend on ρ and z , which cover (isotropically) the meridional plane. Note that the static and axially symmetric electro-vacuum region can always be described in this form.

For the Weyl metric (3), the curvature matrix R_B^A assumes a simple block-diagonal form $\text{diag}(R_1, R_2)$, where R_1 and R_2 are 3×3 matrices. For electro-vacuum spacetimes, R_B^A is traceless and thus its six eigenvalues sum to zero. For vacuum spacetimes, $R_1 = R_2$ in addition, so we are only left with three eigenvalues that can be expressed as

$$\kappa_1 = \frac{1}{2} [R^{t\rho}{}_{t\rho} + R^{tz}{}_{tz} + \sqrt{(R^{t\rho}{}_{t\rho} - R^{tz}{}_{tz})^2 + 4(R^{t\rho}{}_{tz})^2}], \quad (4)$$

$$\kappa_2 = \frac{1}{2} [R^{t\rho}{}_{t\rho} + R^{tz}{}_{tz} - \sqrt{(R^{t\rho}{}_{t\rho} - R^{tz}{}_{tz})^2 + 4(R^{t\rho}{}_{tz})^2}], \quad (5)$$

$$\kappa_3 = R^{t\phi}{}_{t\phi} = R^{\rho z}{}_{\rho z} \quad (6)$$

(so they are independent of u^μ). Specifically, they are, together with the respective eigenvectors n^γ , solutions of the equation

$$E_\gamma^\alpha n^\gamma = -\kappa n^\alpha.$$

For the vacuum case, the range of possibilities is quite restricted. Because the eigenvalues add up to zero, they cannot all be of the same sign. Recalling the original equation of geodesic deviation, it can be expected that the geodesics should diverge in regions where two of the eigenvalues are positive, whereas convergence should prevail where two of them are negative. As $\kappa_1 > \kappa_2$ clearly, it is not possible that $\kappa_1 < 0$ and $\kappa_2 > 0$, so one can specify that there are just two “diverging” cases of $(\kappa_1, \kappa_2, \kappa_3)$: $(++-)$ and $(+-+)$. Sota et al. (1996) conjectured—and also illustrated using examples—that the $(++-)$ region can be expected to induce more instability, because the geodesics there diverge within the meridional (ρ, z) plane, whereas in the $(+-+)$ region the divergence is restricted solely to Killing directions, which should not be that important for the tendency toward chaos.

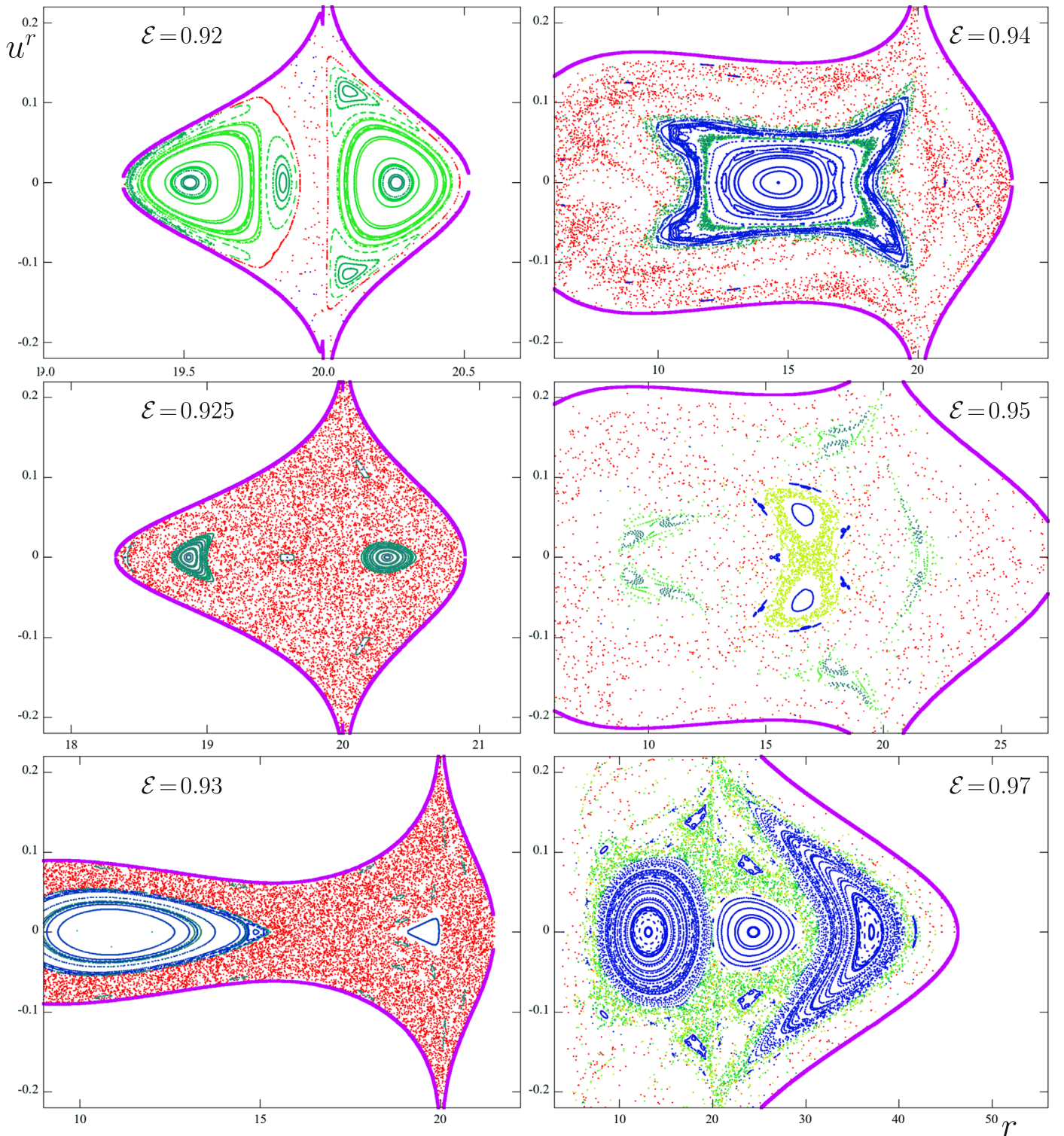


Figure 3. Similar type of Poincaré diagram to those in previous two figures, now showing dependence on the specific energy of geodesics \mathcal{E} (its values are again given in the plots). The ring mass and radius are $\mathcal{M} = 0.5 M$, $r_{\text{ring}} = 20 M$, and geodesics have angular momentum $\ell = 3.75 M$.

For the case with a nonzero electromagnetic field, like for the MP spacetimes, the submatrices R_1 and R_2 differ, but we have checked that in our case the eigenvalues of each of these submatrices almost exactly sum to zero, and that the unstable regions determined by their respective sets of eigenvalues almost exactly coincide (in pairs). Therefore, it is

in fact sufficient to analyze just the three eigenvalues of R_1 (for example) and proceed similarly as in the vacuum (there again exist just two types of unstable regions).

In order to test the criterion, we thus localize, for a given metric and geodesics with given constants of motion, the potentially unstable regions (according to the above

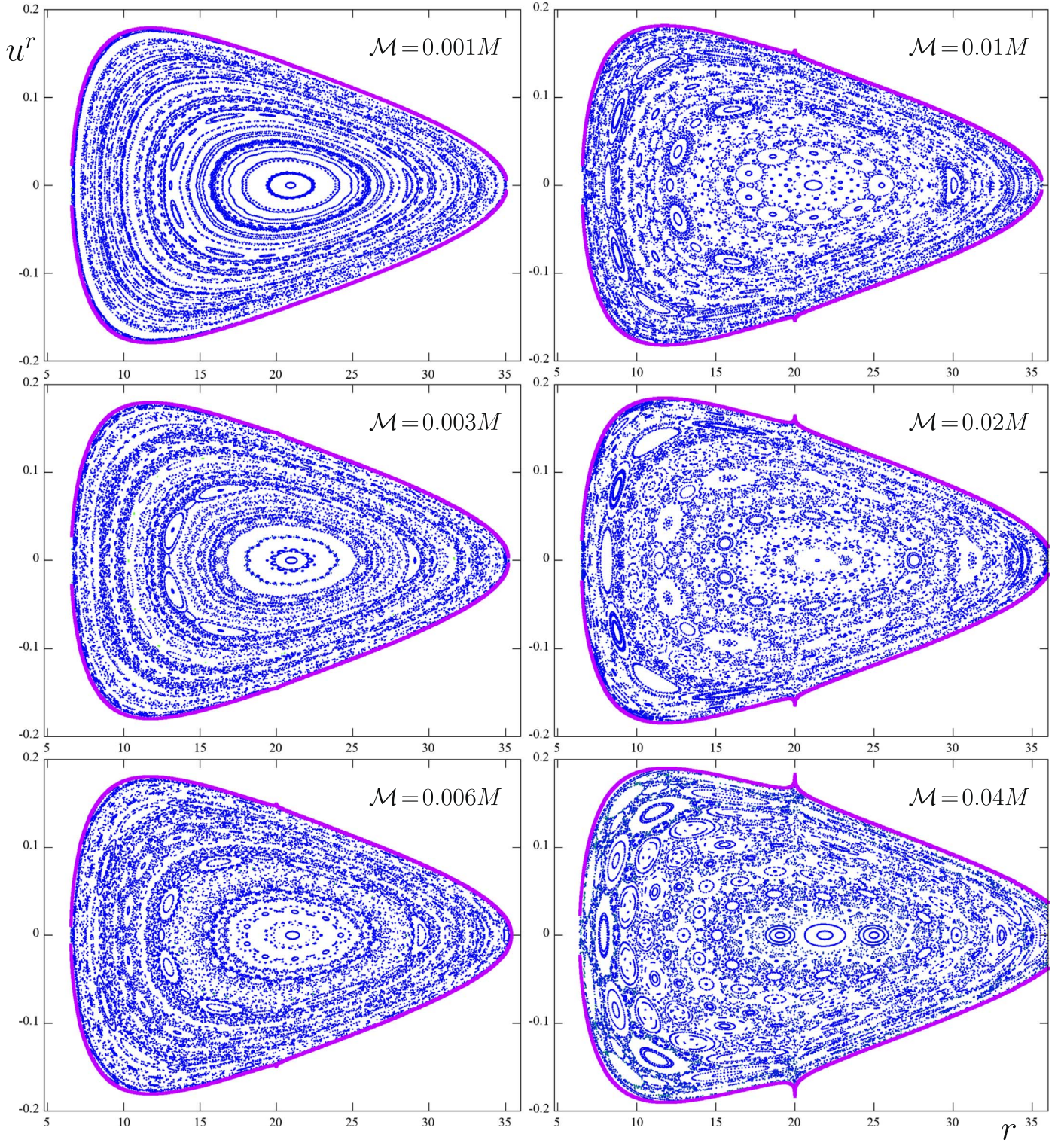


Figure 4. Counterpart of Figure 1 obtained for geodesics in the field of an extreme Reissner–Nordström black hole encircled by a Majumdar–Papapetrou ring. Parameters r_{ring} , ℓ , and \mathcal{E} (and also \mathcal{M} , as indicated in the plots) are chosen the same way as in the Schwarzschild + Bach–Weyl ring case.

eigenvalues), check whether and “how much” of the phase-space volume accessible to the geodesics they occupy (and so can affect the latter), and finally compare the resulting prediction with the numerical integration of geodesics (visualized, e.g., on Poincaré diagrams). Let us recall here that the accessible region is given by the normalization of the four-velocity $g_{\mu\nu}u^\mu u^\nu = -1$, which for our metric (3) can be

rewritten as

$$e^{2\lambda}[(u^\rho)^2 + (u^z)^2] = \mathcal{E}^2 - N^2(1 + N^2\ell^2/\rho^2), \quad (7)$$

where $\mathcal{E} := u_t$ and $\ell := u_\phi$ are the specific energy and azimuthal angular momentum with respect to infinity, conserved along any geodesic. Clearly, the right-hand side has to be

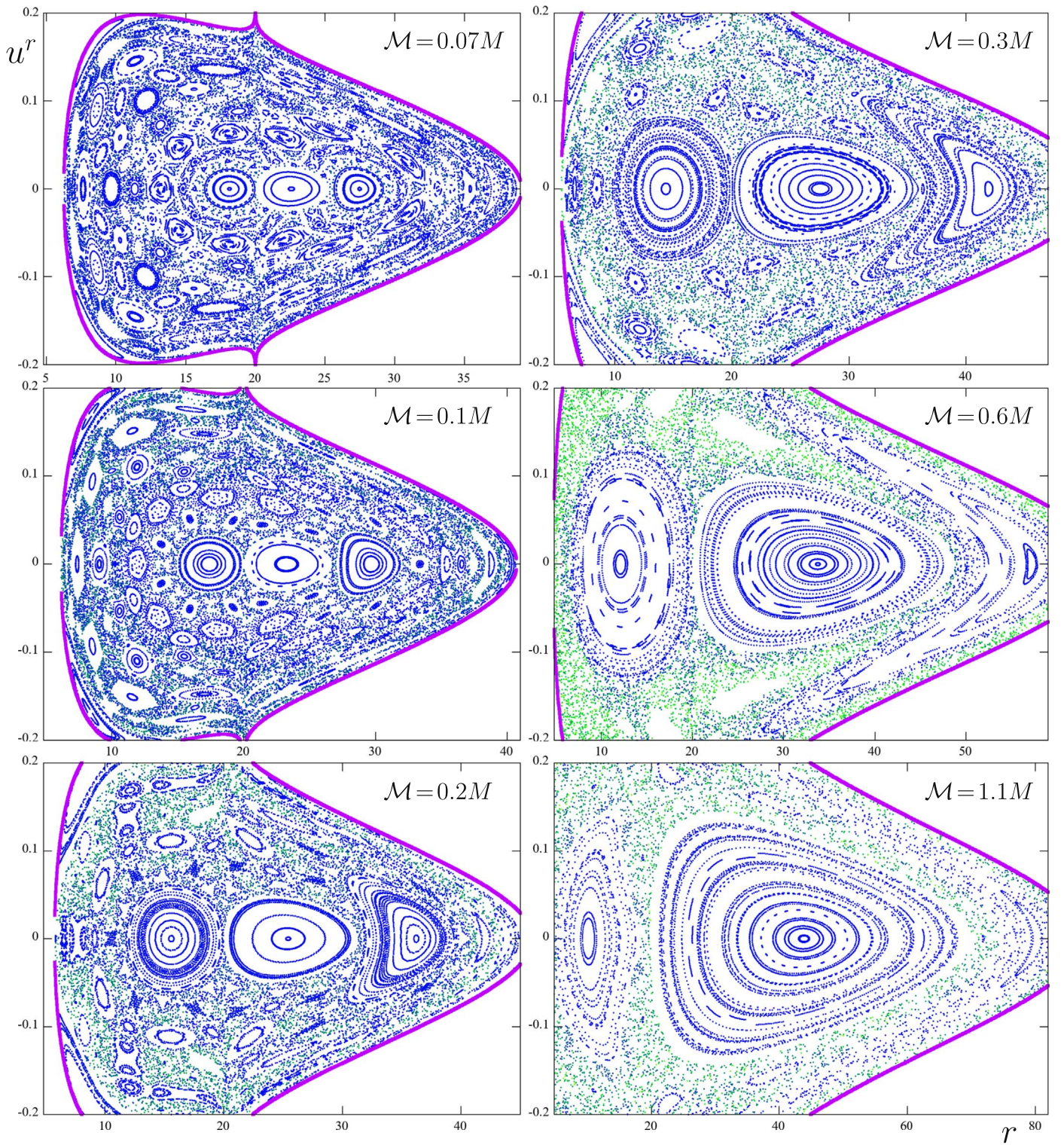


Figure 4. (Continued.)

nonnegative, and this fixes the region where the geodesics with a given \mathcal{E} and ℓ are bound to.

3. Extreme RN Black Hole and the MP Ring

We will check how the geometric criterion works for a time-like geodesic flow in the static and axisymmetric background of an extreme RN black hole surrounded, in a concentric

manner, by a homogeneous circular thin ring also bearing an extremal charge (its charge density is the same as the mass density). Both sources belong to a wider class of MP solutions, a subclass of Weyl spacetimes⁴ with properties fully

⁴ The basic properties of the entire Weyl class of spacetimes were given in previous papers of this series, mainly in the first one, so we do not repeat them here.

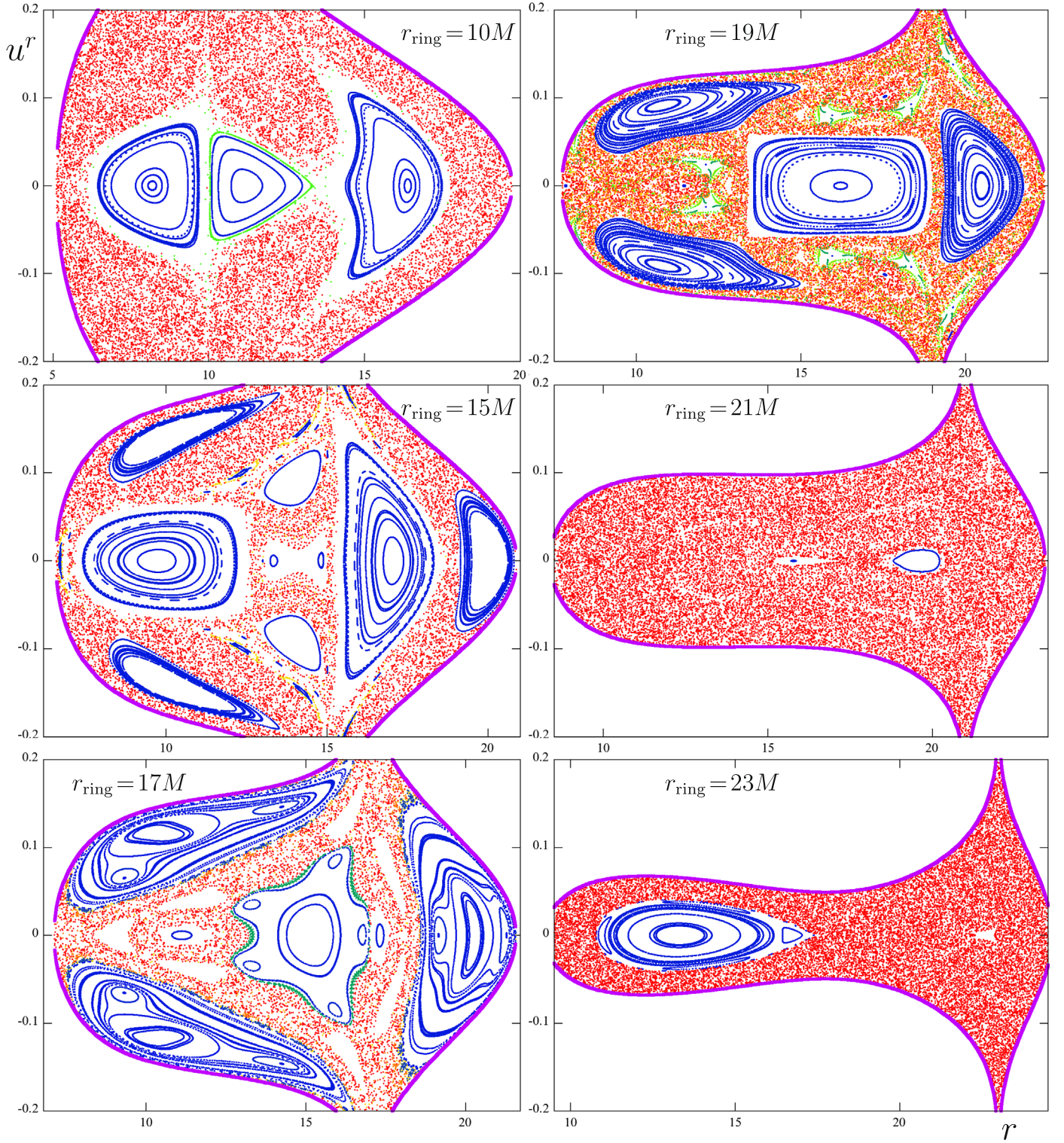


Figure 5. Counterpart of Figure 2 obtained for geodesics in the field of an extreme Reissner–Nordström black hole encircled by a Majumdar–Papapetrou ring. Parameters \mathcal{M} , ℓ , and \mathcal{E} (and also r_{ring} , as indicated in the plots) are chosen the same way as in the Schwarzschild + Bach–Weyl ring case.

represented by just one function, the lapse N , the second Weyl-metric function λ being zero. Hence, the Weyl form of the MP metric

$$ds^2 = -N^2 dt^2 + N^{-2}(\rho^2 d\phi^2 + d\rho^2 + dz^2). \quad (8)$$

For the extreme RN black hole, the lapse function is given by

$$\frac{1}{N} = 1 + \frac{M}{\sqrt{\rho^2 + z^2}}, \quad (9)$$

while for the MP ring it is given by

$$\begin{aligned} \frac{1}{N} &= 1 + \frac{\mathcal{M}}{2\pi} \int_0^{2\pi} \frac{d\phi'}{\sqrt{\rho^2 + b^2 - 2b\rho \cos(\phi - \phi') + z^2}} \\ &= 1 + \frac{2\mathcal{M}K(k)}{\pi l_2}, \end{aligned} \quad (10)$$

where b stands for the ring's Weyl radius and \mathcal{M} for its total mass (we write it in calligraphic font to distinguish it from the black hole mass M),

$$l_{1,2} := \sqrt{(\rho \mp b)^2 + z^2},$$

and

$$K(k) := \int_0^{\pi/2} \frac{d\alpha}{\sqrt{1 - k^2 \sin^2 \alpha}}$$

is the complete elliptic integral of the first kind, with modulus and complementary modulus

$$k^2 := 1 - \frac{(l_1)^2}{(l_2)^2} = \frac{4b\rho}{(l_2)^2}, \quad k'^2 := 1 - k^2 = \frac{(l_1)^2}{(l_2)^2}.$$

Note that the second term of Equation (10) represents the (minus) Newtonian potential of a homogeneous infinitesimally thin ring.

The basic properties of the MP-ring spacetime were studied in Semerák (2016). We showed there that it has quite reasonable properties in comparison with other static axisymmetric ring solutions, mainly in comparison with the BW ring. Most notably and in contrast to the BW ring, the MP ring is locally cylindrical, so it is the same from all “local latitudinal” directions. Actually, as for every Weyl-type solution, the gravitational potential ν (thus lapse) can be taken from the Newtonian treatment (because it is given by the same Laplace equation in both cases) and no surprise occurs at this level, but the second metric function λ (which has no Newtonian counterpart) can seriously deform the spacetime; the BW ring is an example. For the MP ring, on the contrary, $\lambda = 0$, so the field is completely represented just by the potential ν itself, and there is no additional deformation.

3.1. Superposition of the Sources

For a general Weyl-type solution, the Einstein equations imply that the potential ν has to satisfy

$$\nu_{,\rho\rho} + \frac{\nu_{,\rho}}{\rho} + \nu_{,zz} = e^{-2\nu}[(\Phi_{,\rho})^2 + (\Phi_{,z})^2], \quad (11)$$

where Φ is the electrostatic potential. For the MP subclass of solutions, this potential is related to the gravitational potential ν by

$$\Phi = e^\nu + \text{const},$$

so the above equation becomes

$$\nu_{,\rho\rho} + \frac{\nu_{,\rho}}{\rho} + \nu_{,zz} = (\nu_{,\rho})^2 + (\nu_{,z})^2. \quad (12)$$

This is equivalent to the equation

$$N_{,\rho\rho} + \frac{N_{,\rho}}{\rho} + N_{,zz} = \frac{2}{N}[(N_{,\rho})^2 + (N_{,z})^2] \quad (13)$$

for $N \equiv e^\nu$ and can be rewritten as a Laplace equation for $1/N$,

$$(1/N)_{,\rho\rho} + \frac{1}{\rho}(1/N)_{,\rho} + (1/N)_{,zz} = 0. \quad (14)$$

Hence, adding two solutions of the MP type means linearly superposing their $1/N$. Together with the requirement that $N \rightarrow 1$ at spatial infinity, the superposition of the extreme RN black hole with the MP ring is thus described by the total value

$$\frac{1}{N} = 1 + \frac{M}{\sqrt{\rho^2 + z^2}} + \frac{2\mathcal{M}K(k)}{\pi l_2}. \quad (15)$$

4. Geodesic Dynamics in the Field of the RN Black Hole Encircled by the MP Ring

We will first examine, on Poincaré sections, whether the dynamics of bound time-like geodesics in the field of the RN black hole encircled by the MP ring differs significantly from the dynamics in the field of the Schwarzschild black hole encircled by the BW ring, studied in Semerák & Suková (2010). The Poincaré diagrams represent sets of transitions of the particles across the equatorial plane in the (r, u') axes. Each diagram corresponds to some particular parameters of the source (mass and radius of the ring/disk, the black hole mass representing just a mass scale) and some particular values of the constant of geodesic motion; all geodesics followed in any diagram start in the equatorial plane, just from different r and u' (the mesh of initial values being chosen so that the diagram is reasonably filled).

In order to make the Poincaré diagrams more explanatory, we color the orbits according to their MEGNO value—one of the simplest Lyapunov-type indicators, quantifying the rate of orbital divergence. It was explained and employed in Suková & Semerák (2013), so let us just briefly repeat that it is defined by

$$Y(\tau) = 2 [\text{FLI}(\tau) - \overline{\text{FLI}}(\tau)] \ln(10), \quad (16)$$

where the FLI and its time average are calculated from the norm of a separation vector Δx^μ between two neighboring orbits in configuration space (i.e., from their momentary proper distance),

$$\text{FLI}(\tau) = \log_{10} \frac{\sqrt{|g_{\mu\nu} \Delta x^\mu \Delta x^\nu|}(\tau)}{\sqrt{|g_{\mu\nu} \Delta x^\mu \Delta x^\nu|}(0)}, \quad (17)$$

$$\overline{\text{FLI}}(\tau) = \frac{1}{\tau} \int_0^\tau \text{FLI}(s) ds, \quad (18)$$

τ being proper time. Also, the time-average value of MEGNO is often practical,

$$\bar{Y}(\tau) = \frac{1}{\tau} \int_0^\tau Y(s) ds. \quad (19)$$

The main advantage of MEGNO is that in the limit of very long proper time, it approaches the value of 2 for every quasi-periodic regular orbit (or a somewhat higher value for orbits which are regular but pass very close to unstable phase-space structures like resonances or hyperbolic points), whereas it grows linearly for chaotic orbits. It is thus very helpful in distinguishing between regular and chaotic trajectories.

For an easy comparison of the new (RN+MP) figures with the old (Schw+BW) ones, we repeat some of the plots provided, for the latter configuration, in Semerák & Suková (2010), because

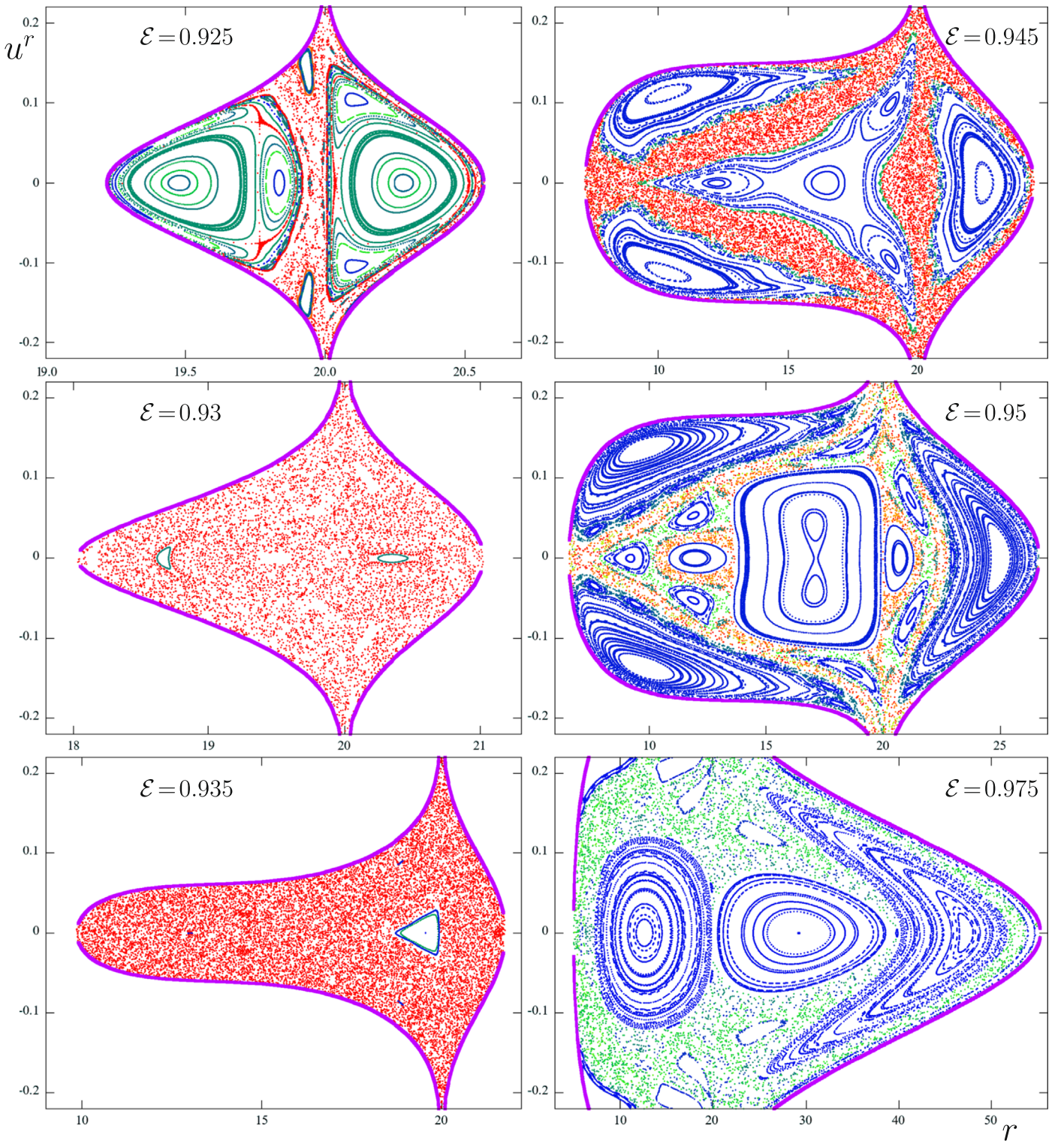


Figure 6. Counterpart of Figure 3 obtained for geodesics in the field of an extreme Reissner–Nordström black hole encircled by a Majumdar–Papapetrou ring. Parameters \mathcal{M} , ℓ , and r_{ring} are chosen the same way as in the Schwarzschild + Bach–Weyl ring case, while the sequence of energies \mathcal{E} (indicated in the plots) is slightly different (namely, 0.925, 0.93, 0.935, 0.945, 0.95, and 0.975, instead of 0.92, 0.925, 0.93, 0.94, 0.95, and 0.97).

there they were drawn in just black and white (here we color them in the same way as the new plots obtained for the other sources). The Schwarzschild + BW ring case is thus covered by Figures 1–3 while the RN + MP ring case is covered by Figures 4–6.

The figures indicate that, qualitatively, the geodesic dynamics in both fields do not differ much, the main difference

actually being that in the case of the RN + MP ring, the phase-space region where a particle with a given energy and angular momentum can exist (it is indicated by the violet boundary in the figures) tends to be closed, whereas in the case of the Schwarzschild + BW ring it often opens toward the horizon, so in this latter case some particles fall to the black hole and only partially contribute to the diagram. For such trajectories, it is

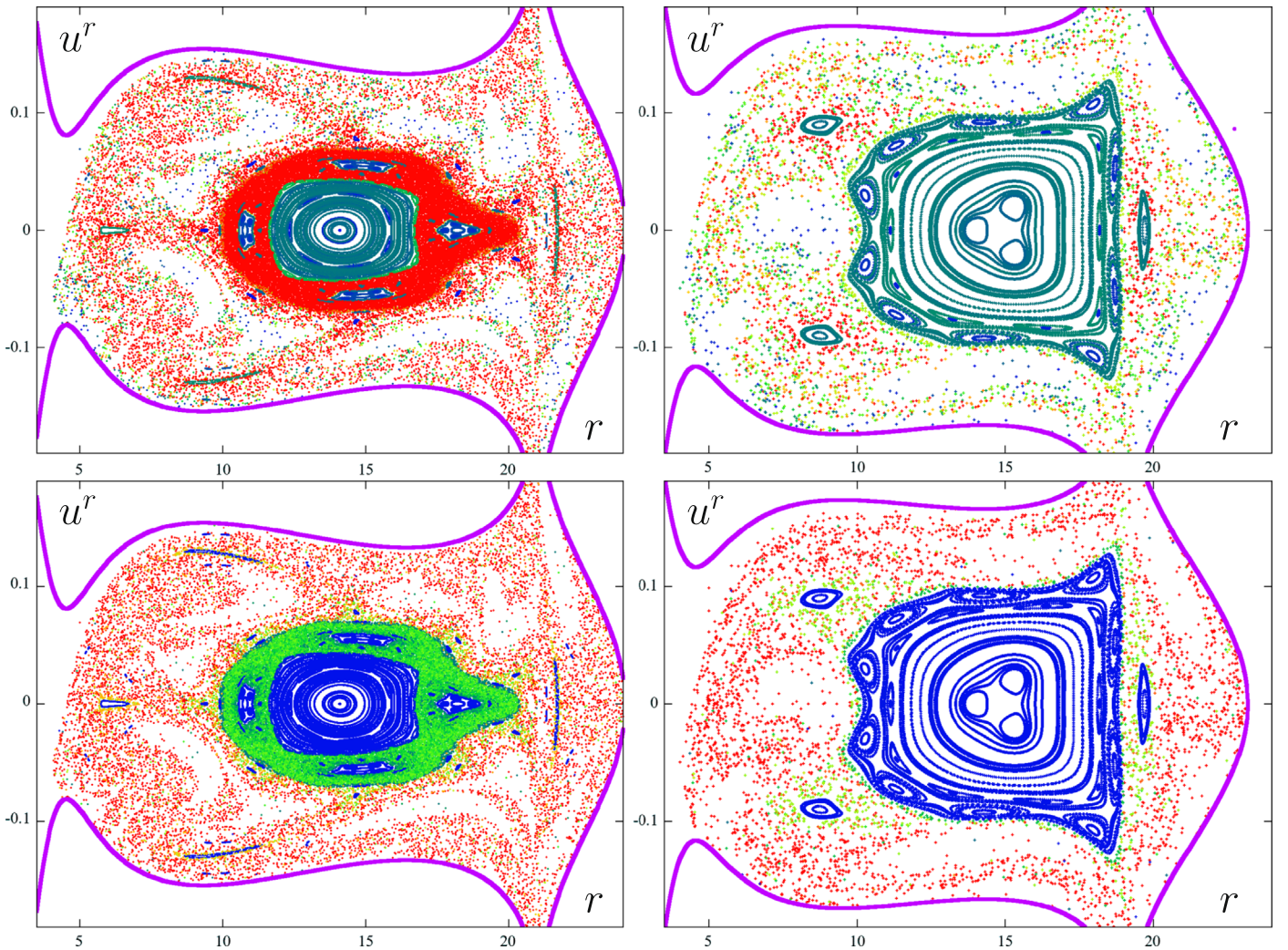


Figure 7. Two illustrations of the difference between MEGNO and what we call “relative MEGNO” (MEGNO achieved by a given orbit divided by the proper time over which the orbit has been followed). Both columns of Poincaré diagrams show the dynamics of geodesics with constants of motion $\mathcal{E} = 0.94$, $\ell = 3.75 M$ in the field of a Schwarzschild black hole encircled by the Bach–Weyl ring of mass $\mathcal{M} = 0.5 M$; in the left/right column, the ring has radius $r_{\text{ring}} = 19 M / 21 M$, respectively. The top row is colored by MEGNO (dark blue to red corresponds to its ranging from “zero” to more than 30), while the bottom row is colored by relative MEGNO (ranging, through the same color spectrum, from zero to more than 0.0008); no additional shift is applied. The coloring is strongly dependent on where one places its limits, but, according to our experience, the relative MEGNO distinguishes more certainly between the regular and chaotic trajectories: in the top row, what is clearly a chaotic sea still contains many regular-looking (green or even blue) points, while, on the other hand, the regular island is not as strictly blue as in the bottom (despite trying to adjust the coloring suitably). Also note that the orbits that stick to the regular center in the case shown on the left are assessed more adequately in the bottom plot, namely, as being less chaotic than the chaotic sea.

difficult to determine the degree of their chaoticity, because the indicators of orbital divergence (like MEGNO) only approach their relevant values at asymptotic times. For this reason, we have instead employed a “relative MEGNO”—the MEGNO divided by the proper time for which a given trajectory had been followed. Such a modified parameter has turned out to better indicate the degree of chaoticity. Namely, for chaotic trajectories, MEGNO typically grows linearly with time, so if a chaotic particle escapes from the system (e.g., falls to the black hole) too soon, its MEGNO reaches a lower value than what would correspond to its actual nature. This is particularly important in our case, because when the accessible region opens toward the black hole, the particles from its outer parts leave first, and these exactly are typically the most chaotic (“chaotic sea”). See Figure 7 for two examples of how the relative MEGNO is a more precise indicator than the original MEGNO itself.

The color scale employed, for the relative MEGNO value, in all figures ranges from 0 to 0.0005 (blue to red, in the spectral order), which means, roughly speaking, that blue and possibly green indicate regular orbits, while red marks the most chaotic ones.

5. Numerical Check of the Sota–Suzuki–Maeda Curvature Criterion

We will naturally check the relevance of the Sota–Suzuki–Maeda criterion by computing phase-space portraits of the geodesic system (as recorded in Poincaré sections again) for different parameters and by comparing them with the location of the “diverging” regions identified by eigenvalues of the tidal matrix determined by the Riemann tensor. Note that in the following figures we draw the accessible region in red and the unstable regions given by the geometric criterion in light blue

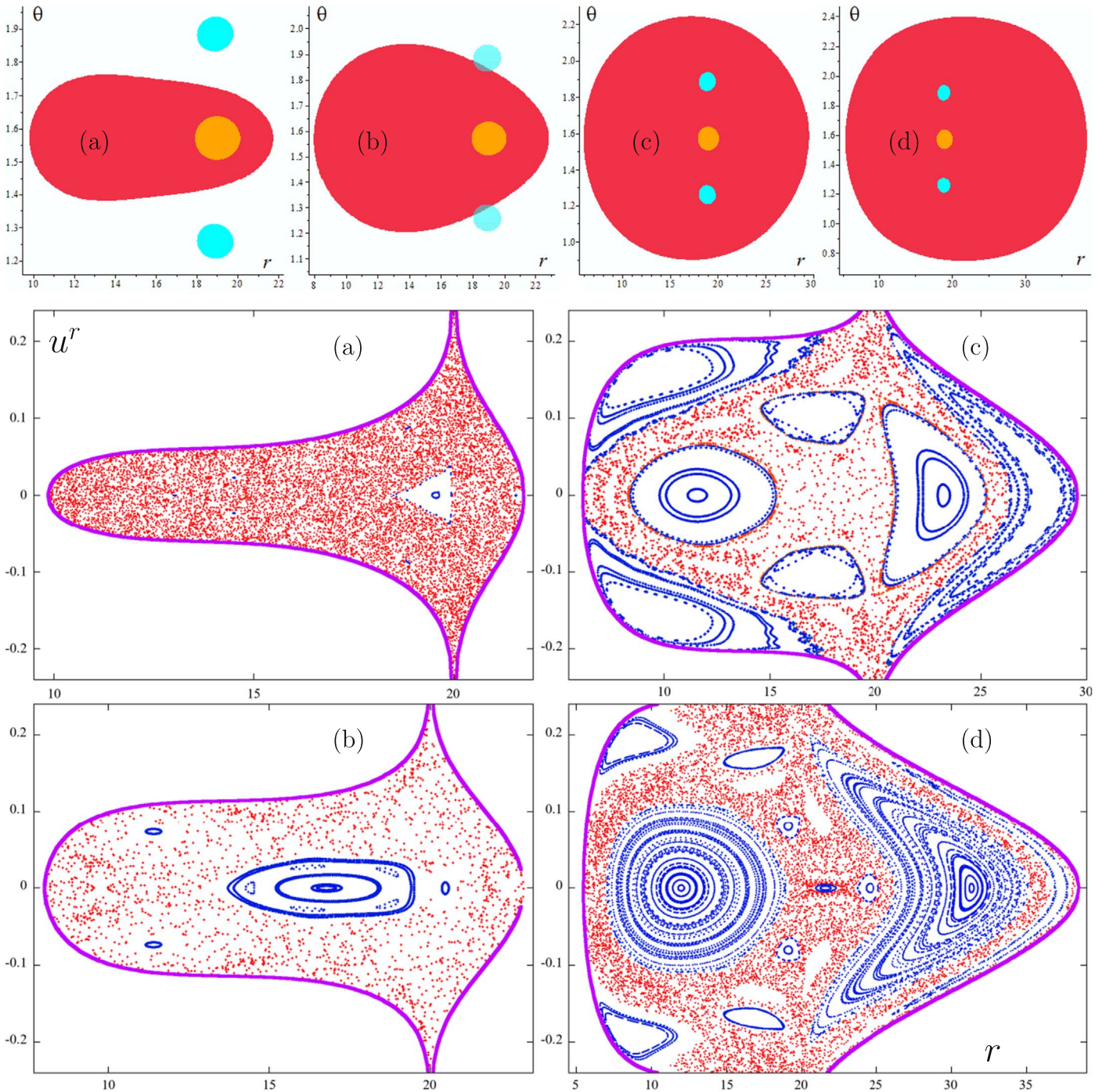


Figure 8. Comparison of the geometric criterion with the actual geodesic dynamics portrayed on Poincaré diagrams, performed, for four different particle energies, in the field of a Reissner–Nordström black hole encircled by the Majumdar–Papapetrou ring with mass $\mathcal{M} = 0.5 M$ and radius $r_{\text{ring}} = 20 M$. All geodesics have $\ell = 3.75 M$, with energies (a) $\mathcal{E} = 0.935$, (b) $\mathcal{E} = 0.940$, (c) $\mathcal{E} = 0.955$, and (d) $\mathcal{E} = 0.965$. Top row: regions determined as unstable by the geometric criterion (plotted in the r, θ plane); red is the accessible region, and light blue and orange are the unstable regions (with $++-$ and $+++$ signs of the curvature eigenvalues, respectively). Bottom two rows: equatorial Poincaré diagrams of geodesics (plotted in the (r, u^r) plane); transition points are colored by MEGNO—dark blue are regular orbits and red are chaotic orbits.

(with $++-$ signs of the curvature eigenvalues) and in orange (with $+++$ signs).

Figure 8 shows the comparison between the unstable-region maps given by the geometric criterion and Poincaré sections for geodesics in the field of the RN black hole encircled by the MP ring. The plots are given for several different values of the geodesic specific energy \mathcal{E} . For low energies, the unstable regions are seen to occupy most of the accessible region, which

should indicate rather strong inclination to chaos; with increasing energy, the unstable regions remain the same, while the accessible region grows, indicating attenuation of chaoticity. The Poincaré diagrams confirm such a tendency, though perhaps not as clearly as one could expect.

Figure 9 shows the same comparison for geodesics in the field of the Schwarzschild black hole encircled by the BW ring, this time for several different radii of the ring. All unstable

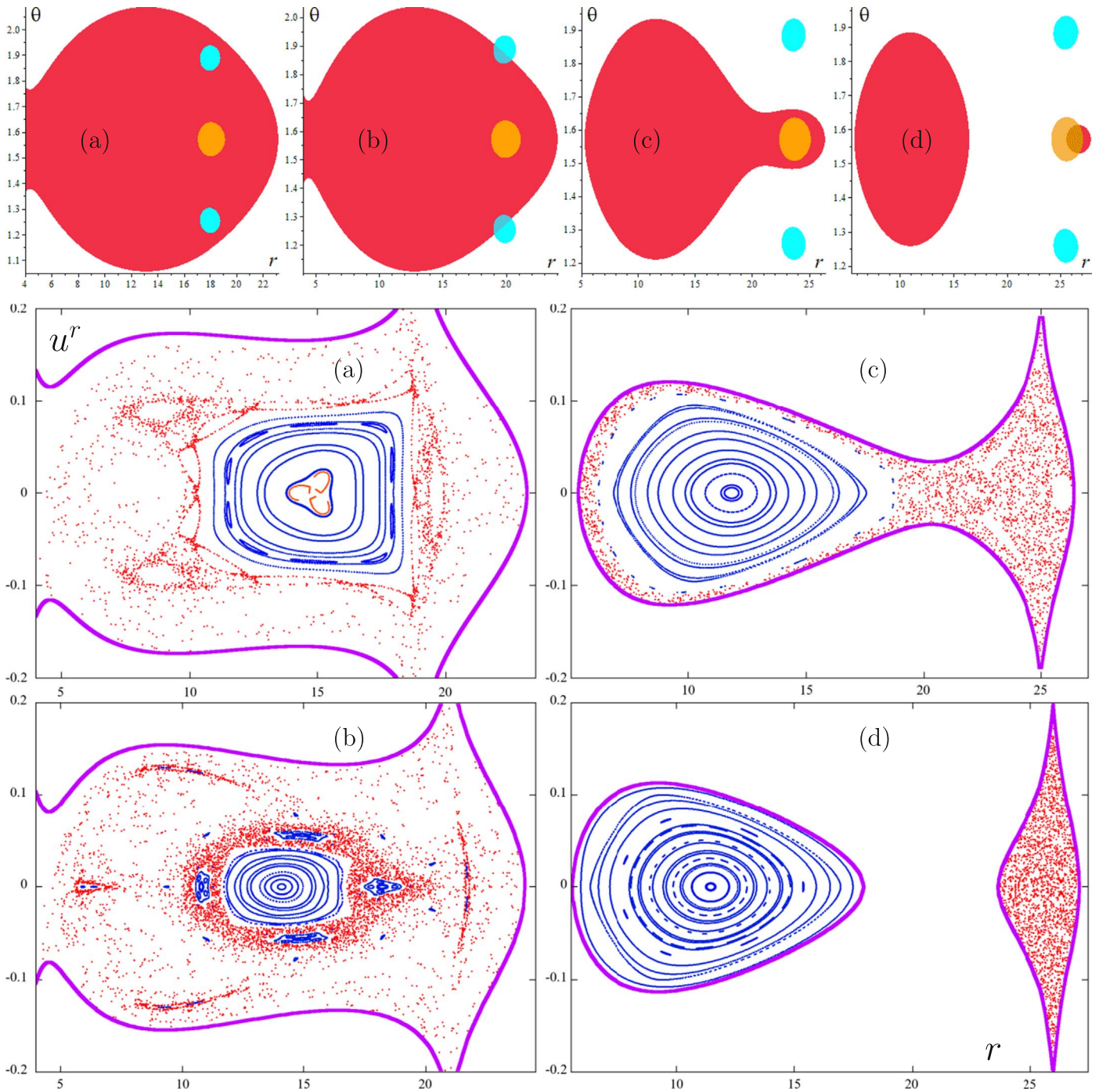


Figure 9. Comparison of the geometric criterion with the actual geodesic dynamics portrayed on Poincaré diagrams, performed in the field of a Schwarzschild black hole encircled by the Bach–Weyl ring with mass $\mathcal{M} = 0.5 M$ and with four different radii: (a) $r_{\text{ring}} = 19 M$, (b) $r_{\text{ring}} = 21 M$, (c) $r_{\text{ring}} = 25 M$, and (d) $r_{\text{ring}} = 27 M$. All geodesics have $\ell = 3.75 M$ and $\mathcal{E} = 0.94$. Top row: regions determined as unstable by the geometric criterion (plotted in the (r, θ) plane); red is the accessible region, and light blue and orange are the unstable regions (with $+++$ and $+++$ signs of the curvature eigenvalues, respectively). Bottom two rows: equatorial Poincaré diagrams of geodesics (plotted in the (r, u^r) plane); transition points are colored by MEGNO—dark blue are regular orbits and red are chaotic orbits.

regions are seen to first (for $r_{\text{ring}} = 19 M$) lie completely inside the accessible region. Later—with increasing ring radius—the blue regions leave the accessible region; at some point, the accessible region splits into two, the lower one (closer to the black hole) completely devoid of unstable regions, and the upper one (located below the ring) almost “covered by” the orange unstable region. This nicely agrees with what one sees in Poincaré’s diagrams. In particular, the last one

($r_{\text{ring}} = 27 M$) shows a completely regular lower part of the accessible region and a completely chaotic upper part. A similar observation can be inferred from a series showing dependence on the ring mass (not shown here).

In previous papers of this series, we also considered a thin equatorial disk around a Schwarzschild black hole, specifically the one obtained by inversion of some member of the Morgan–Morgan counter-rotating family. We have now also tested the

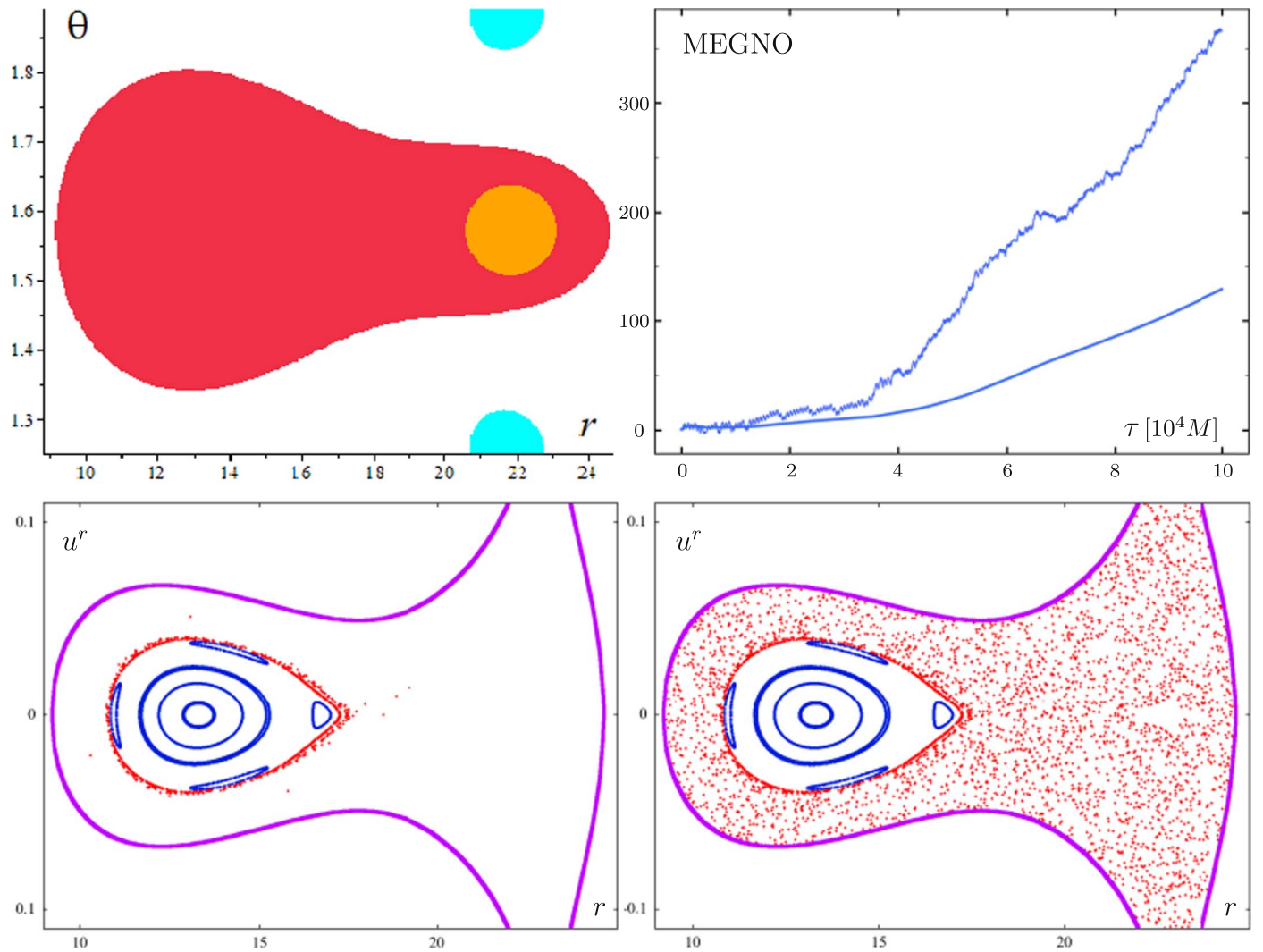


Figure 10. Example of a situation where the geometric criterion works very well: an orbit that sticks to a large regular island for quite some time, but then begins to cross the “orange” unstable region (as identified by the criterion) and fills the entire accessible zone in a chaotic manner. It happens in the field of the extreme Reissner–Nordström black hole encircled, at $r_{\text{ring}} = 23 M$, by the Majumdar–Papapetrou ring of mass $\mathcal{M} = 0.5 M$. The plotted geodesics have $\mathcal{E} = 0.94$ and $\ell = 3.75 M$. Poincaré diagrams with a regular island (blue) and chaotic orbit (red) are at the bottom—the left one captures the first $3.5 \times 10^4 M$ of that orbit’s proper time and the right one covers about $10 \times 10^4 M$ of proper time. The orbit turns from “sticky” to strongly chaotic after hitting the unstable region (the orange one at top left, lying within the red accessible region) at $\tau \simeq 3.5 \times 10^4 M$; this is clearly seen, at top right, in the increase of the slope showing how the MEGNO of the orbit grows (the bottom curve there shows the mean MEGNO).

geometric criterion in such a gravitational background and have not found agreement with the actual dynamics as good as that for the rings. This may seem surprising because the disks, being spatially two-dimensional, are more physical (as relativistic sources) than one-dimensional rings, so intuition can be expected to work better for them. However, what is probably disturbing are the transits of particles across the disk, because the field jumps across the disk in the perpendicular direction, like across any source layer.⁵ As an example of a situation where the criterion does not work well, see Figure 11. There, no unstable regions occur within the accessible lobe, yet the Poincaré diagram still contains chaotic layers.

⁵ If the particles hit the ring or come very close to its vicinity, their motion is just terminated, because the ring represents a curvature singularity and, therefore, has to be “excised” by the code. On the other hand, the disk is regular and there is no reason to stop the particles there (and we ignore any possible mechanical interaction)—in fact, they typically cross the disk repeatedly at some stage of their motion.

5.1. Quantification of the Geometric-criterion Effectiveness

The locations of unstable regions and the corresponding Poincaré sections provide only a summary picture of what should in fact arise from local behavior (restricted to certain spatial regions and thus happening only during certain intervals of time). In order to at least roughly quantify the comparison, it is desirable to track down whether, when, for how long, or at least how often a specific particle has crossed the unstable region and, on the other hand, how the chaos-indicating parameters have evolved along its trajectory. For this purpose, we will compute the time evolution of MEGNOs for some particular orbits and, conversely, record how much of their proper time these orbits spend in crossing the “diverging” regions determined by the curvature (or/also how many times they have crossed such regions). The degree of correlation between these quantities could indicate whether or not the criterion is effective. One might of course consider a more sophisticated quantity like an average of the λ_1 and λ_2 values

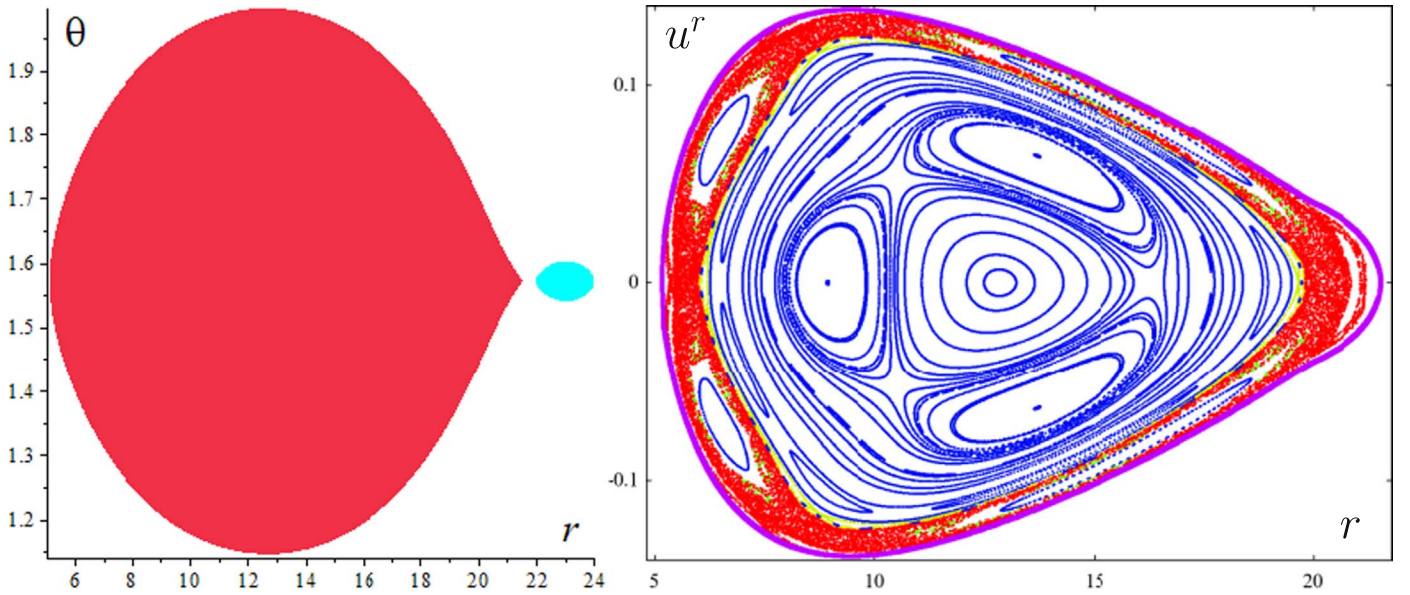


Figure 11. Example of a situation when the curvature criterion does not “predict” the dynamics properly: geodesics around a Schwarzschild black hole encircled, at $r_{\text{disk}} = 20 M$, by the inverted first Morgan–Morgan disk of mass $\mathcal{M} = 0.5 M$. The geodesics have energy $\mathcal{E} = 0.953$ and angular momentum $\ell = 3.75 M$. The left plot shows the only unstable region (light blue) outside of the accessible region (red), yet the Poincaré section on the right still reveals a chaotic layer at the accessible-region boundary (region filled with red transitions).

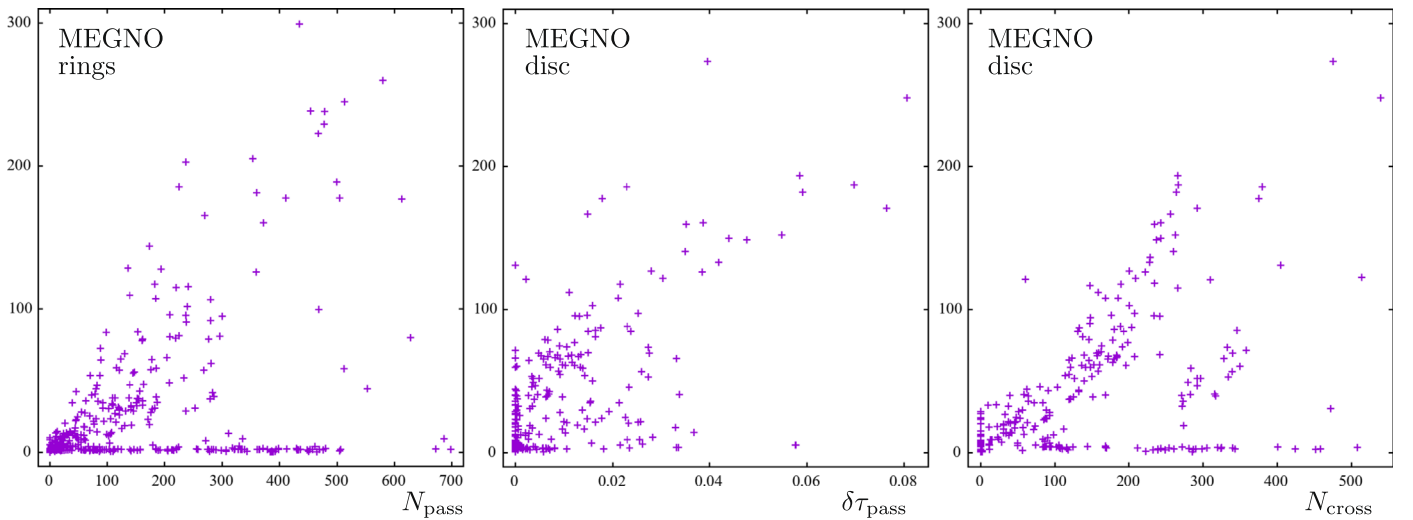


Figure 12. Terminal MEGNO of the orbits we followed, as plotted against simple numbers connected with possible destabilizing circumstances: in the left plot, it is the number of passages through unstable regions N_{pass} (included are the results obtained for both ring superpositions we consider); the middle and right plots concern the inverted first Morgan–Morgan disk and MEGNO is plotted there against the relative proper time the orbits spend in the unstable regions ($\delta\tau_{\text{pass}}$) and against how many times they crossed the disk (N_{cross}). There is apparently some correlation, but there are also many “exceptions.”

along the orbit, but we will adhere to the simple possibilities in the former.

It is not a problem to find either regular or chaotic orbits for which the geometric criterion works very well. However, such orbits that start in a “regular” region but, after some time, get to a region where the geometric criterion indicates instability (and then, possibly, leave to the regular part of phase space again) are the most interesting. An example of such an orbit is given in Figure 10: the figure contains four plots, the first showing the location of unstable regions within the accessible part of the phase space, the second showing the evolution of MEGNO with proper time, and the third and fourth showing the Poincaré sections recorded before hitting the unstable region for the first time (left) and recorded for the entire trajectory (right). The

geometric criterion works perfectly here, namely, the orbit is almost regular before and quite chaotic after it hits the unstable region, with the MEGNO slope really increased at the time when the unstable region is first entered.

However, there exist orbits whose character the criterion does not predict correctly. For example, we noticed that this can be the case for orbits that are regular but lie close to a resonant or hyperbolic torus (this is typically indicated by MEGNO going asymptotically to a constant value larger than 2; see Maffione et al. 2011). These orbits may spend quite some time in an unstable region, so the geometric criterion incorrectly predicts their chaotic nature. To give a specific example, we found a regular orbit with an asymptotic MEGNO of 3.054, for which the relative proper time spent in an unstable

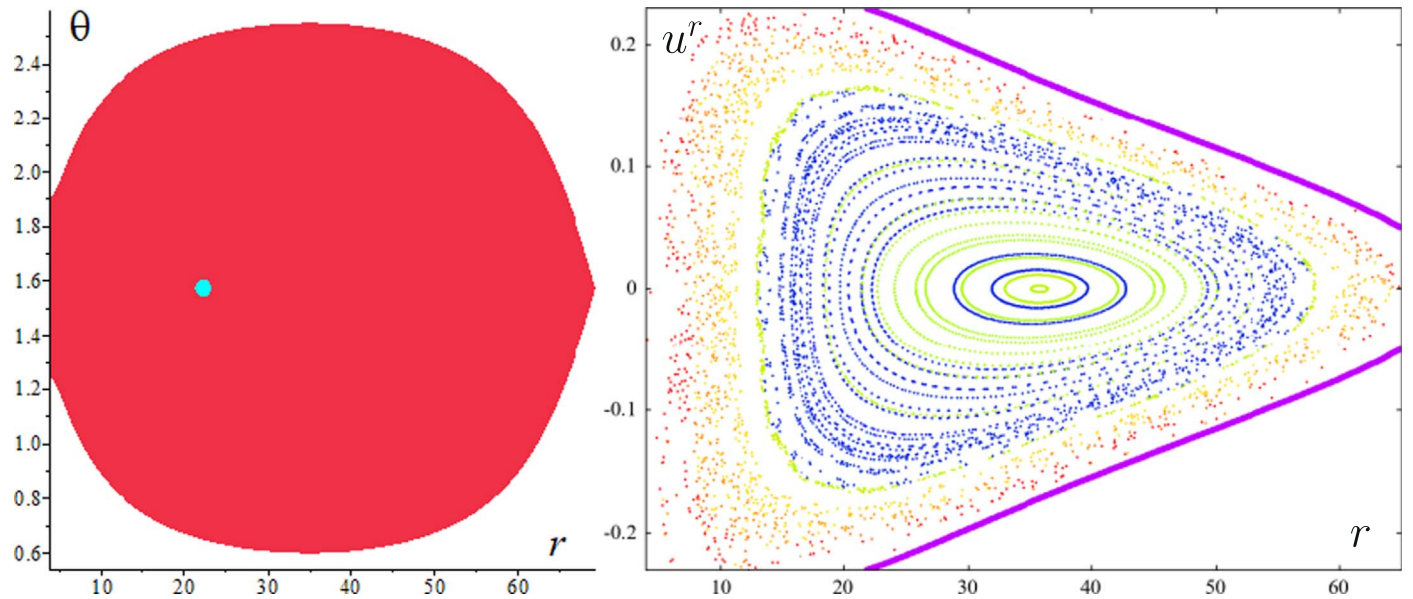


Figure 13. Example of a situation when neither the curvature criterion nor the incidence of disk crossings suggests the proper picture of the dynamics: geodesics (with energy $\mathcal{E} = 0.98$ and angular momentum $\ell = 3.75M$) around a Schwarzschild black hole encircled, at $r_{\text{disk}} = 19.493M$, by the inverted first Morgan–Morgan disk of mass $\mathcal{M} = 0.5M$. The left plot shows that the unstable region (light blue) does occur inside the accessible region (red), but it is so tiny that the computed geodesics practically do not cross it, yet the Poincaré section on the right still reveals a wide chaotic layer at the outskirts of the accessible region (yellow to red transitions). On the other hand, almost all the orbits crossed the disk repeatedly, yet there is still a notable regular island (blue to green transitions).

region was 0.0323. (This value may seem small, but we should add that even the most chaotic orbits we studied spend just several percent of their proper time in unstable regions. See the middle plot of Figure 12 where the MEGNO is plotted against the total relative time the orbits spend in the unstable regions to get an idea from there about typical values.) The above experience may indicate that unstable structures of the phase space (hyperbolic orbits) are not correlated with the presence of unstable regions given by the curvature.

Another piece of information on the effectiveness of the geometric criterion can be provided by plotting, for a large number of orbits, the terminal value of MEGNO achieved in a simulation against the number of passages through the unstable region(s) determined by the criterion—see Figure 12 where such a plot is shown (it is the left one there) containing orbits around both centers considered above (RN black hole encircled by the MP ring and Schwarzschild black hole encircled by the BW ring); a similar result can be obtained for the correlation between the MEGNO and the relative proper time the orbits spend in the unstable regions. In general, MEGNO really grows with the number of passages, but there exist orbits with many passages yet with MEGNO remaining small (the points along the horizontal axis). These, in particular, include the orbits mentioned in the previous paragraph. The figure—and our experience in general—can be summarized so that the geometric criterion seems to be necessary, but not sufficient for the geodesic dynamics to be chaotic (there are no orbits clustered along the vertical axis).

Turning now to the case of a Schwarzschild black hole encircled by a thin disk (the inverted first Morgan–Morgan disk in particular), we saw that for this gravitational background the geometric criterion even fails to be a necessary condition for chaos (see example in Figure 11). In order to test our conjecture that it may be due to the crossings of the disk by geodesics, let us check a different correlation, that between the achieved value of MEGNO and the number of times it passed across the

disk. Figure 12 (right two plots) confirms that such a correlation really turns out to work better (like, for example, in the situation represented in Figure 11, where the curvature criterion failed). However, this correlation is not always valid—for example, in Figure 13 almost all geodesics cross the disk many times, but the Poincaré section still contains a large regular island. In the left plot of that figure, the “prediction” of the curvature criterion is also shown: a tiny blue unstable region lies inside the accessible region, but is almost never hit by any of the particles (yet there is a chaotic orbit at the outer parts of the accessible region, reaching a MEGNO value equal to 31.11).

As a certain summary of results obtained for the Schwarzschild black hole encircled by the inverted first Morgan–Morgan disk, we again plot, for several tens of orbits, their terminal values of MEGNO against the relative proper time spent in regions predicted to be unstable (middle plot of Figure 12) and also against the number of crossings through the disk (right plot of Figure 12). The correlation is clearly stronger for the second plot, but even there one sees cases of many crossings yet low MEGNO values. The thin-disk case would thus require a more detailed study, but it is possible that that would also not lead to any clear conclusion, as also experienced in the literature. Let us add, on the other hand, that we have not encountered the case when the unstable region(s) would fill almost the entire accessible lobe yet the dynamics would still be completely regular (this would be the strongest counterexample to the geometric criterion).

6. Concluding Remarks

Full geodesic integrability is one of the remarkable features of spacetimes admitting (or actually “generated by” in a mathematical sense) a nondegenerate closed conformal Killing–Yano two-form, as recently summarized thoroughly by Frolov et al. (2017). Such spacetimes are said to possess “hidden symmetries”; they are

necessarily of curvature type D and represent, essentially, those of isolated stationary black holes (loosely speaking, those of the Kerr type).⁶ The integrability is ensured by the existence of the “fourth” integral of the (electro-)geodesic motion (aside from the momentum norm and the integrals following from stationarity and axisymmetry); in a Newtonian case, its counterpart represents the “third” integral and its existence was, e.g., investigated by Hénon & Heiles (1964).

In the present paper, we continued to study how a deviation from the above Kerr-like ideal destabilizes the geodesic dynamics. Restricting to the simple case of spherically symmetric black holes, we considered their perturbations due to a thin ring or disk, specifically, the BW ring around a Schwarzschild black hole, the MP (extremely charged) ring around an extreme RN black hole, and the inverted first disk of the counter-rotating Morgan–Morgan family around the Schwarzschild black hole. One new point has been the inclusion of the electrically charged case, motivated by the much more reasonable behavior of geometry in the vicinity of the MP ring (than around the BW ring). In spite of the quite different nature of spacetime in that case (it is no longer a vacuum), the geodesic dynamics appears to go through, with growing strength of the perturbation, stages similar to those of the vacuum, Schwarzschild + BW case. More profound differences could instead be expected if the additional source broke the reflection symmetry.

Let us mention some recent publications on chaotic motion around perturbed black holes. Kopáček & Karas (2014) analyzed perturbation exerted on charged particles by an external large-scale magnetic field inclined with respect to the black hole rotation axis. Liu et al. (2017) studied test motion around a Schwarzschild black hole perturbed by a shell of dipoles, quadrupoles, or octupoles, and Li & Wu (2019) considered a Schwarzschild black hole immersed in a magnetic field. Nag et al. (2017) observed, within a pseudo-Newtonian treatment, that the spacetime dragging due to the center’s (black hole) rotation has an attenuating effect on geodesic chaos. Lukes-Gerakopoulos & Kopáček (2018) used recurrence analysis for a particle inspiralling while emitting gravitational waves in a deformed Kerr field and showed that the character of the motion can be recognized even if noise is present in the observed signal. Let us also mention Bannikova (2018), who studied the motion in the field of a torus (as approximated by a thin ring), inspired by the case of ring galaxies (Hoag’s objects).

Another one of our points has been to check the validity of one of the curvature-based estimates of chaos, from Sota et al. (1996). We confirmed that it is neither necessary nor sufficient, although it mostly works as a useful indicator. It should be admitted here that our fields contain singularities (thin sources themselves, namely rings or disks), which is not a situation where one would guess that the geometric criteria for geodesic chaos could work reliably, so next we might either focus on motion kept away from these irregularities, or consider more regular (extended) sources, e.g., a thick toroid instead of a thin ring. The relation between thick toroids and their infinitesimally thin ring limits is definitely worth further study, and similarly is the influence of field irregularities caused by thin

matter configurations, mainly in order to judge how major an error one introduces when employing such sources as approximation of real astrophysical bodies. This does not only concern infinitesimally thin rings (we have a clear experience that the “contact” of particles with such a ring is strongly destabilizing), but also razor-thin layers (disks) that generate a jump in the normal field. As shown by Vieira & Ramos-Caro (2016) within a Newtonian treatment, in the latter case the destabilization need not be that strong, especially for orbits crossing such a thin disk where there still typically exists an approximate “third” integral of motion (besides energy and angular momentum).

Other plans for the future include using other methods like Melnikov’s integral or the basin-boundary analysis, and, needless to say, more interesting (and astrophysically more adequate) spacetimes involving rotation.

We thank the support from grants GACR-17/06962Y (L.P., P.S.) and GACR-17/13525S (O.S.) of the Czech Science Foundation. We also acknowledge that our numerics is based on a code written two decades ago by one of O.S.’s students, M. Žáček.

ORCID iDs

P. Suková  <https://orcid.org/0000-0002-4779-5635>
O. Semerák  <https://orcid.org/0000-0002-1272-6779>

References

- Anosov, D. V., & Sinai, Ya. G. 1967, *RuMaS*, 22, 103
Bach, R., & Weyl, H. 1922, *MatZe*, 13, 134
Bannikova, E. Y. 2018, *MNRAS*, 476, 3269
Biesiada, M. 1995, *CQGr*, 12, 715
Chen, S., Wang, M., & Jing, J. 2016, *JHEP*, 2016, 82
Frolov, V. P., Krtouš, P., & Kubizňák, D. 2017, *LRR*, 20, 6
Hénon, M., & Heiles, C. 1964, *AJ*, 69, 73
Kopáček, O., & Karas, V. 2014, *ApJ*, 787, 117
Li, D., & Wu, X. 2019, *Eur. Phys. J. Plus*, 134, 96
Liu, L., Wu, X., & Huang, G. 2017, *GReGr*, 49, 28
Lukes-Gerakopoulos, G., & Kopáček, O. 2018, *IJMPA*, 27, 1850010
Maffione, N. P., Giordano, C. M., & Cincotta, P. M. 2011, *IJNLM*, 46, 23
Nag, S., Sinha, S., Ananda, D. B., & Das, T. K. 2017, *Ap&SS*, 362, 81
Ramasubramanian, K., & Sriram, M. S. 2001, *PhRvE*, 64, 046207
Saa, A. 2004, *AnPhy*, 314, 508
Semerák, O. 2016, *PhRvD*, 94, 104021
Semerák, O., & Suková, P. 2010, *MNRAS*, 404, 545
Semerák, O., & Suková, P. 2012, *MNRAS*, 425, 2455
Sota, Y., Suzuki, S., & Maeda, K. 1996, *CQGr*, 13, 1241
Stránský, P., & Cejnar, P. 2015, *JPhA*, 48, 125102
Suková, P., & Semerák, O. 2013, *MNRAS*, 436, 978
Szczęsny, J., & Dobrowolski, T. 1999, *AnPhy*, 277, 161
Szydłowski, M. 1993, *PhLA*, 176, 22
Szydłowski, M. 1994, *JMP*, 35, 1850
Szydłowski, M. 1997, *IJMPD*, 6, 741
Szydłowski, M., Heller, M., & Sasin, W. 1996, *JMP*, 37, 346
Szydłowski, M., & Krawiec, A. 1996, *PhRvD*, 53, 6893
Vieira, R. S. S., & Ramos-Caro, J. 2016, *CeMDA*, 126, 483
Vieira, W. M., & Letelier, P. S. 1996b, *CQGr*, 13, 3115
Witzany, V., Semerák, O., & Suková, P. 2015, *MNRAS*, 451, 1770
Wu, X. 2009, *JGP*, 59, 1357
Yurtsever, U. 1995, *PhRvD*, 52, 3176

⁶ It should be specified that the black holes have to be non-accelerating. Actually, there exist black hole type-D spacetimes that do not possess hidden symmetries, and thus their geodesics are in general not completely integrable. They are described by “C-metric-type” solutions (a subclass of the Plebański–Demiański metrics), and in the accelerating case their geodesics can really show chaotic behavior (see Chen et al. 2016).